Microstructural, multilevel simulation of notch effect in ferritic ductile cast iron under low cycle fatigue

Microstructural, multilevel simulation of notch effect in ferritic ductile cast iron under low cycle fatigue

Collini L., Pirondi A.

Department of Engineering and Architecture, University of Parma, Parco Area delle Scienze 181/A, 43124 Parma – Italy

Luca.collini@unipr.it; alessandro.pirondi@unipr.it

Abstract

Triaxiality of stress affects damage and failure of ductile metals. In mechanical components, triaxiality increases in the proximity of a notch, or, at the microstructural level, due to inclusions or voids. In this work, the effect of triaxiality on the LCF of ductile cast iron is investigated by a multilevel approach, homogenizing the response of a microstructural model which feeds a notched specimen. Moving from micro- to macro-scale, results indicate that triaxiality shorten the fatigue life. Thus, the notch effect on fatigue life of cast iron can be explained in terms of the combined effects of microstructure and applied triaxiality.

Keywords: *Stress triaxiality; RVE modelling; hysteresis energy; ductile cast iron, low-cycle fatigue.*

Nomenclature

σ^0	size of yield surface
$\sigma\|_0$	yield stress at zero plastic strain
Q_∞	maximum change of size of yield surface
b	rate of yield surface size change
C	kinematic hardening modulus
γ	decreasing rate of kinematic hardening
$\boldsymbol{\alpha}$	backstress tensor
Δw	strain energy per hysteresis loop
N_0	number of cycles to failure
c_i	i = 1,…,4 ferritic matrix fatigue damage parameters
N_G	nodule count
d_G	nodule average diameter
ψ_G	graphite volume fraction
E_G	graphite Young's modulus
L_{EL}	Finite element characteristic length
D	scalar damage variable
η	stress triaxiality at the microscale, $\eta = -p/q$
p	first stress invariant (hydrostatic pressure)
q	second stress invariant
ΔE_i	i-th component of the cyclic strain amplitude at the meso-scale (i = 1, 2, 3 in principal strain direction)
E^{pl}	equivalent cyclic plastic strain
Σ_i	i-th component of the stress at the meso-scale
$\boldsymbol{E}$	strain tensor at the meso-scale
$\boldsymbol{\Sigma}$	stress tensor at the meso-scale
$\boldsymbol{A}$	backstress tensor at the meso-scale
T	stress triaxiality rate at the mesoscale

Y	Young's modulus of the DCI
K', n'	parameters of the R–O model of cyclic curve
$\bar{\sigma}_f'$, $\bar{\varepsilon}_f'$, b, c	parameters of the Manson-Coffin-Basquin law of the DCI at $T = 1/3$
Σ'_f, E'_f, b', c', k_1, k_2	parameters of the triaxiality-modified Manson-Coffin-Basquin law
N_f	number of cycles to failure
N_f^*	number of cycles to failure modified to account for triaxiality
C_i	$i = 1,\ldots,4$ mesoscopic fatigue damage parameters of the DCI
W	failure strain energy per volume (homogenized)
$\frac{\Delta\bar{\varepsilon}}{2}$	nominal strain amplitude at the net section of RNB models

1. Introduction

Ductile Cast Iron (DCI) is very versatile iron-based alloy produced by casting in large quantities worldwide. Only the European foundries associated to The European Foundry Association (CAEF), that share just a 15 % of the global market, yields 5.38 billions of kilograms of DCI per year [1]. DCI has a greater strength and ductility than gray (lamellar) cast iron, that makes it a material suitable for a variety of applications including pipes, automotive components, wheels, gear boxes, pump housings, machine frames for the wind-power industry, and many more.

Several of these applications are subjected to fatigue loading, often in presence of notches and discontinuities, making the estimation of service life of a DCI component a challenge, still nowadays. Notches locally change stresses, thus triaxiality of stress T, that is defined as the ratio between the first, p, and the second stress invariant q (or hydrostatic stress and Von Mises equivalent stress, respectively). The triaxiality is long known to strongly influence the quasi-static failure behavior of ductile metals [2]. In general, the higher the triaxiality the lower the strain to failure, while at low and negative triaxialities the Lode angle was shown to revert this trend in some cases [3], even in a porous media [4].

The main model types, such as porous plasticity [5] and Continuum Damage Mechanics [4,6], homogenize damage on the mesoscale, i.e. the smallest size where damage effects can be considered

independent from the size itself. In multiphase materials therefore, the question of what is the mesoscale size with respect to the size and distribution of phases is not straightforward, as well as how the damage mechanism in matrix material can be influenced by the presence of the other phase(s) for a given triaxiality at the mesoscale. Additionally, since engineering materials work most under fatigue loading, the question of how damage develops under these conditions is of utmost importance.

This work tries to investigate this interrogative by a multiscale modelling of a DCI notched component subjected to fatigue. As known, DCI is a multiphase material due to the presence graphite particles immersed into the ferritic α-matrix. Since the nodule-matrix interface can have some influence on the mechanical behavior [7–9], especially in compression under cyclic loading, graphite nodules are here modeled within the matrix. Typical dimensions of such spheroids are of some tenths of microns, and interparticle distance is about 3–5 times the diameter. Number and distance of graphite spheroids, together with the matrix microstructure formation, are also determining the mechanical behavior of DCI in terms of strength and ductility, as already evidenced by many previous works, also by the present authors [10,11]. Ferritic matrix is extremely ductile in nature and promotes the plastic deformation and the accumulation of dislocations, both under static and cyclic loading, but above all, these particles, evenly dispersed in the matrix in percentage from 8 to 15% in volume, behave as stress concentrators. Around the nodules the triaxiality can locally raise well above 1/3, as demonstrated experimentally [12] and, recently, numerically [13,14]. This can determine not only the increasing of cavity dimension, but also the change of the matrix failure mechanism, from collapse to coalescence of cavities incorporating nodules [4,15]. As a result, ductility can drastically change, from microstructural (ferrite can even present cleavage) to mesoscopic level [14,16].

The DCI “material system” is particularly prone to be studied by a unit cell or, in general, by a Representative Volume Element (RVE) approach, and the same will be shown in this work. Numerous works in literature simulated the DCI under monotonic and cyclic loading by the unit cell approach, testing its reliability and finding a correlation between fatigue life and triaxiality under monotonous and cyclic loading [17–21], and a promising agreement with LCF behavior at triaxiality 1/3 [22]. By the micromechanical approach, a multilevel analysis is usually adopted: the mesoscale, with mesoscopic stress and strains Σ_{ij}-E_{ij}, and the microscale, where microscopic quantities σ_{ij}-ε_{ij} apply. The stress

triaxiality is also expressed in terms of Σ_{ij}, or of σ_{ij}, referring to as mesoscopic and local triaxiality T and η, respectively. Mesoscopic quantities are here manipulated as boundary conditions on the RVE, as specified in Section 3. However, Fig. 1 introduces the scheme of the RVE definition and of the cyclic loading on it under mesoscopic triaxiality control. These define the first two levels of the simulation.

Given the above introduction to the problem formulation, the main aim and novelty of this work is the simulation of the cyclic behavior of DCI in the LCF regime, under different triaxialities. A cubic RVE containing a stochastic population of incoherent graphite particles is modelled, and a cyclic plasticity rule is chosen to define the evolution of the α-matrix response. Damage is incorporated in the matrix constituent, which is the solely designated at concurring the cell failure. The triaxiality at the mesoscale is being varied over the range 0.333–1.0 and a triaxiality-modified Manson-Coffin-Basquin (M-C-B) law is formulated. The study does not limit to analyze the effect of T, but apply the findings to the investigation of a notched "real" specimen where the material model is the homogenized response obtained on the RVE. The expected fatigue life obtained from the modified M-C-B law is then compared with the theoretical one resulting from Neuber's rule at the monoaxial triaxiality T = 1/3. This is the third, macro-scale level of analysis.

The outcomes indicate that the combination of T and microstructure results in a life shortening comparable to the one estimated by Neuber's rule, with the number of reversals to failure corrected for the triaxiality as determined by RVE analysis; in other words, the notch effect on the LCF of ferritic cast iron can be explained in terms of combined triaxiality and microstructure effects, as discussed in the following.

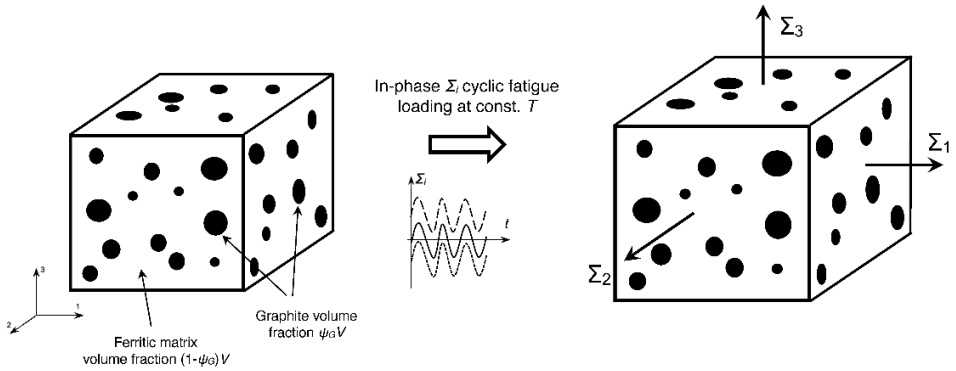

Fig. 1. Cyclic loading and triaxiality control on the RVE model of DCI.

2. Material modeling

A full ferritic DCI belonging to the spheroidal class GJS-400 is here reproduced, with yield strength 250–300 MPa, ultimate strength 400–450 MPa, elongation to failure 15–18%. Fig. 2 shows its typical microstructure. Graphite nodules are characterized in number, size and reciprocal spacing. Failure of the ferritic matrix is being determined by the accumulated energy of the hysteresis loop generated by the cyclic loading, that is controlled in strain amplitude. In order to describe the evolution of the stabilized loop area, a combined nonlinear isotropic/kinematic model of the evolution of the yield surface is chosen, expressed as a function *f*:

$$f(\boldsymbol{\sigma}-\boldsymbol{\alpha}) = \sigma^0 \tag{1}$$

with $\boldsymbol{\alpha}$ the kinematic shift, or backstress, and σ^0 the yield surface size, and the associated plastic flow is

$$\dot{\varepsilon}^{pl} = \frac{\partial f(\boldsymbol{\sigma}-\boldsymbol{\alpha})}{\partial \boldsymbol{\sigma}} \dot{\bar{\varepsilon}}^{pl} = \frac{\partial f(\boldsymbol{\sigma}-\boldsymbol{\alpha})}{\partial \boldsymbol{\sigma}} \sqrt{\frac{2}{3}\dot{\boldsymbol{\varepsilon}}^{pl} : \dot{\boldsymbol{\varepsilon}}^{pl}} \tag{2}$$

where $\dot{\varepsilon}^{pl}$and $\dot{\bar{\varepsilon}}^{pl}$are the plastic flow rate and the equivalent plastic strain rate. The nonlinear isotropic evolution of yield stress σ^0 is expressed by the exponential expression [23]:

$$\sigma^0 = \sigma|_0 + Q_\infty \left(1 - e^{-b\bar{\varepsilon}^{pl}}\right) \tag{3}$$

where $\sigma|_0$ is the initial yield strength, and Q_∞ (maximum change of σ^0 until saturation) and b (evolution rate of σ^0as plastic strain develops) are material parameters. The cyclic evolution of the backstress tensor (kinematic hardening) is:

$$\dot{\boldsymbol{\alpha}} = C\dot{\bar{\varepsilon}}^{pl}\frac{1}{\sigma^0}(\boldsymbol{\sigma}-\boldsymbol{\alpha}) - \gamma\boldsymbol{\alpha}\dot{\bar{\varepsilon}}^{pl} \tag{4}$$

with C (initial kinematic hardening modulus) and γ (rate of the recall term) material parameters. Set of parameters for the matrix, reported here in Tab. 1, refers to a ferritic steel and are taken from literature [24]. In addition, a continuum-based model of damage initiation and evolution is used, based on the accumulation of inelastic hysteresis strain energy per cycle [25]. To each stress reversal, plastic strain is being accumulated, and the number of cycles for damage initiation is:

$$n_0 = c_1 \Delta w^{c_2} \tag{5}$$

where Δw is the strain energy per cycle in MJ/m^3, and c_1 and c_2 are material constants. Once the initiation condition is met, a progressive damage is simulated by degrading the ferrite elastic stiffness and the undamaged stress tensor $\bar{\boldsymbol{\sigma}}$ by the quantity (1–D), where $D \leq 1$ is a damage variable. In turn, the rate of damage at a material point evolves with the number of cycles n by the law:

$$\frac{dD}{dn} = \frac{c_3 \Delta w^{c_4}}{L_{EL}} \tag{6}$$

where c_3 and c_4 again are material, and L_{EL} the element characteristic length, which depends by the mesh sizing. The set of parameters c_i indicated in Tab. 1 is chosen to match experimental strain-controlled LCF tests [26,27], assuming, as for the ductile cast iron itself, that the crack propagation part of the life is the 10% of the total fatigue life [28].

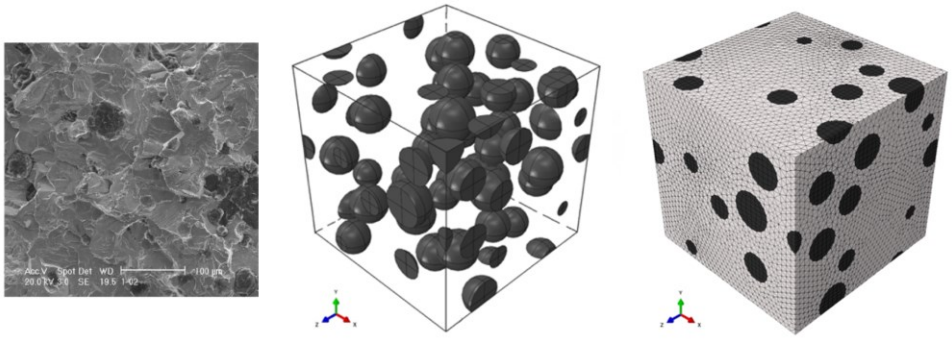

Fig. 2. Fatigue fracture surface and RVE model of DCI, with detail of nodules population and mesh.

The definition of the hysteresis loop, which directly concurs to the initiation and evolution criteria (5) and (6), depends by the calculated stress field, to which the local triaxiality η is related by two contributions: i) the stress concentrations in vicinity of nodule cavities, acting as micro-notches [13,14] and, ii) the imposed triaxiality T at the meso-scale.

Tab. 1. Parameters for the modeling of the ferritic matrix.

E (GPa)	ν	$\sigma\|_0$ (MPa)	Q_∞ (MPa)	b	C (MPa)	γ	c_1	c_2	c_3	c_4
206	0.3	380	49	2	15,000	260	18,201	-1.43	$2.5 \cdot 10^{-6}$	1.5

Regarding the nodules, graphite is brittle and does not show plasticity for none of the observed loading conditions. Nodules' compressive strength is much higher than the tensile, and solidification of graphite can form radial planes in a structure that is not isotropic [29]. The strength at the interface with the α-matrix is scarce. Under cyclic plastic strain and high triaxiality, debonding occurs starting from the application of quite low strain; from this on, nodules contribute in compression only [30], and observed residual (static) strains due to cooling down, which for a 50-micron nodule are elastic and around 0.04-0.06 % [31,32], tends to fade out. So, for the aims of this work nodules are modeled however as isotropic elastic solids with Young's modulus E_G = 15 GPa and ν = 0.22, which are typical values [33,34]. In addition, with the aim of reproducing the non-symmetrical behavior, the ABAQUS© *CAST IRON PLASTICITY model is applied, limiting the elastic range to σ_{lt} = 15 MPa in tension and σ_{lc} = 125 MPa in compression, and assuming the default plastic Poisson's ratio 0.04 [35].

3. Numerical modeling and solution control

The study is conducted with the FE code ABAQUS© on two FE models representing the analysis at the micro and meso-scale:

- the above-mentioned RVE, that is cubic 0.25x0.25x0.25 mm^3 in size containing a stochastic distribution of graphite nodules that mimics the real microstructure at the micro-scale;

- an axisymmetric model of round notched bar specimen (RNB), that reproduces the material response at the macro-scale.

The flow chart of the study in Fig. 3 shows the RVE cyclically loaded in strain control at various T imposed at the meso-scale, and the obtained homogenized behavior described by classical LCF curves that are function of T; the same constitutive law is applied to the RNB reproducing different triaxialities at the notch, and again the LCF response compared to classical analytical Neuber's prediction.

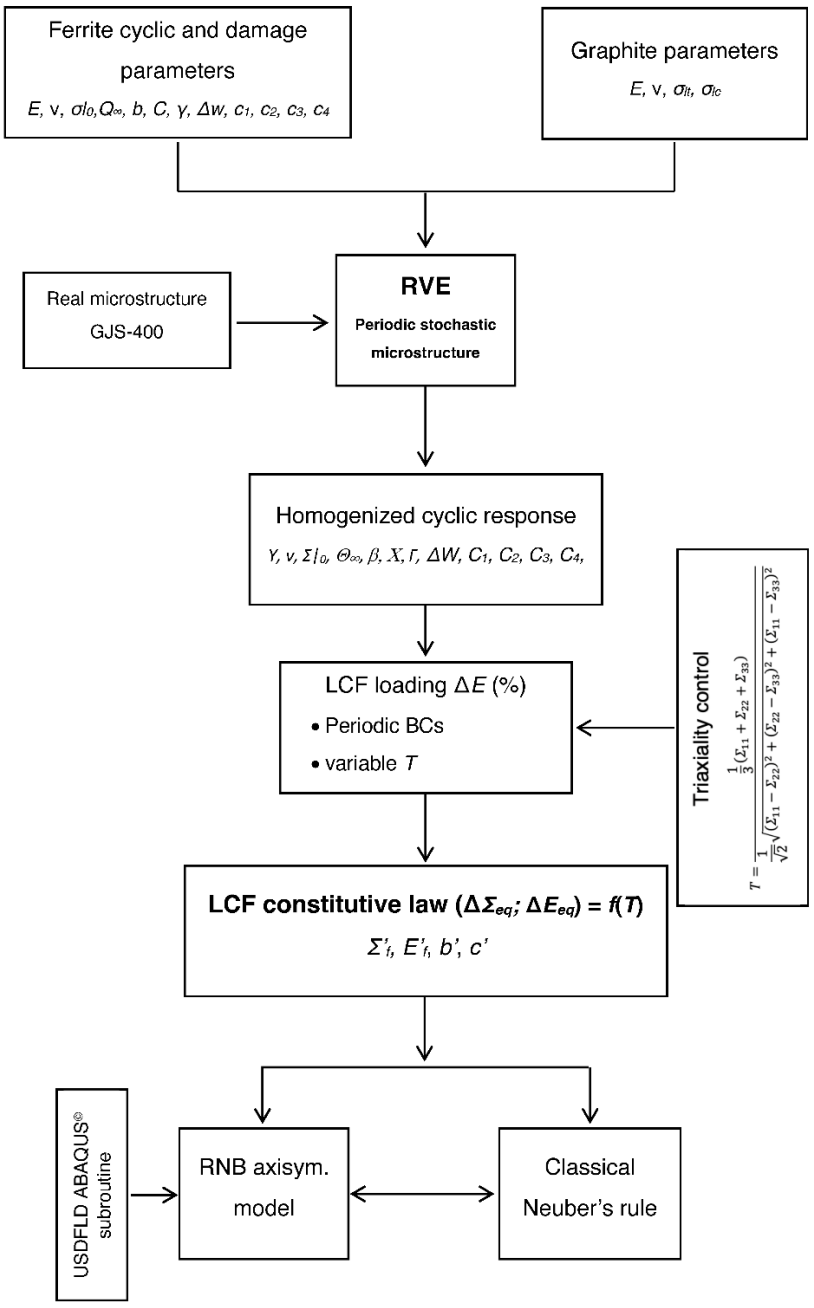

Fig. 3. Flow chart of the study.

3.1. RVE model

Regarding the first model, shown in Fig. 2, the microstructure is automatically generated by the open-source toolbox Mote3D by setting the number of nodules, their average size, standard deviation and clustering. No control is applied to the nodularity, here assumed as 100 %, which is, however, realistic for most of good quality DCIs [11]. The RVE is periodic within geometry and boundary conditions of the opposite faces. Details of the modeling technique are reported in [13,14,22], and essential parameters are recalled in Tab. 2. Linear tetrahedral elements are used for the matrix, with decreasing size in proximity of nodules that are meshed by second order elements; characteristic element length results L_{EL} = 0.01167 mm which is about 1/20 of the RVE side.

Tab. 2. Parameters of the RVE model.

N_G	d_G (μm)	ψ_G (%)	Nodularity	Nodes	Elements/typology	L_{EL} (mm)
49	45±8	13.5	100%	48,529	196,030 C3D4-C3D8R	1.167e-2

FE solution is controlled by the ABAQUS© *DIRECT CYCLING low-cycle fatigue simulation procedure, that uses a combination of Fourier series and time integration of the nonlinear material behavior to obtain the stabilized cycle response. The damage is evaluated at discrete time points along the load history and the solution of these points is used to predict the degradation and evolution of material properties at the next time increment after Δn cycles. Damage due to repeated loading can locally reach the value of 1, simulating the initiation and eventually evolution of damage. However, in this study the RVE is considered failed as it losses 50% in stiffness, calculated as the slope of the elastic part of the hysteresis loops. Loads are applied to a master node as reversal strain amplitudes ΔE_k, where k =1,2,3 denotes the principal directions, see Fig. 1. The 1-direction mesoscopic strain ΔE_1, which is taken as reference, is being varied in the range 0.2–1.2%, while ΔE_2 and ΔE_3 are determined in-phase with ΔE_1 in order to obtain the desired triaxiality T, that is expressed by the reaction forces Σ_i at the master node itself. Reactions are not constant during the cycling, due to the stabilization of plasticity and the onset of damage, hence Σ_i are being evaluated at the 50% of the RVE life.

Four triaxialities are analyzed: uniaxial tension (T = 1/3), plane strain tension (T = 1/√3), equibiaxial tension (T = 2/3), and unitary T. A homogenized material behavior is then defined for the RVE by a set

of equations in the same form of Eqs. (5, 6) representing the damage initiation and evolution at the meso-scale, where this time the coefficients C_1-C_4 vary with T, in order to account for the effect of triaxiality on the fatigue life:

$$N_{0,RVE} = C_1(T)\Delta W^{C_2(T)} \tag{7}$$

$$\left.\frac{dD}{dN}\right|_{RVE} = \frac{C_3(T)\Delta W^{C_4(T)}}{L_{RVE}} \tag{8}$$

where ΔW is the RVE strain energy per cycle, expressed in MJ/m^3, integrated from the simulated hysteresis loop. As a result, different ΔW–N_f (number of cycles to failure) curves are obtained for the different applied T. These curves can be then described in the form of a triaxiality-dependent M-B-C equation.

In order to evaluate $C_1(T)$, $C_2(T)$, the RVE damage initiation is defined taking $N_{0,RVE}$ in Eq. (7) as the number of cycles at which a loss of 5 % in stiffness is recorded. The analysis of $N_{0,RVE}$ vs. the corresponding ΔW at different values of T allowed then the definition of $C_1(T)$, $C_2(T)$. Regarding $C_3(T)$ and $C_4(T)$, a homogenized concept of damage for the whole RVE is taken, $D_{RVE} = 1 - K/K_0$ [25], where

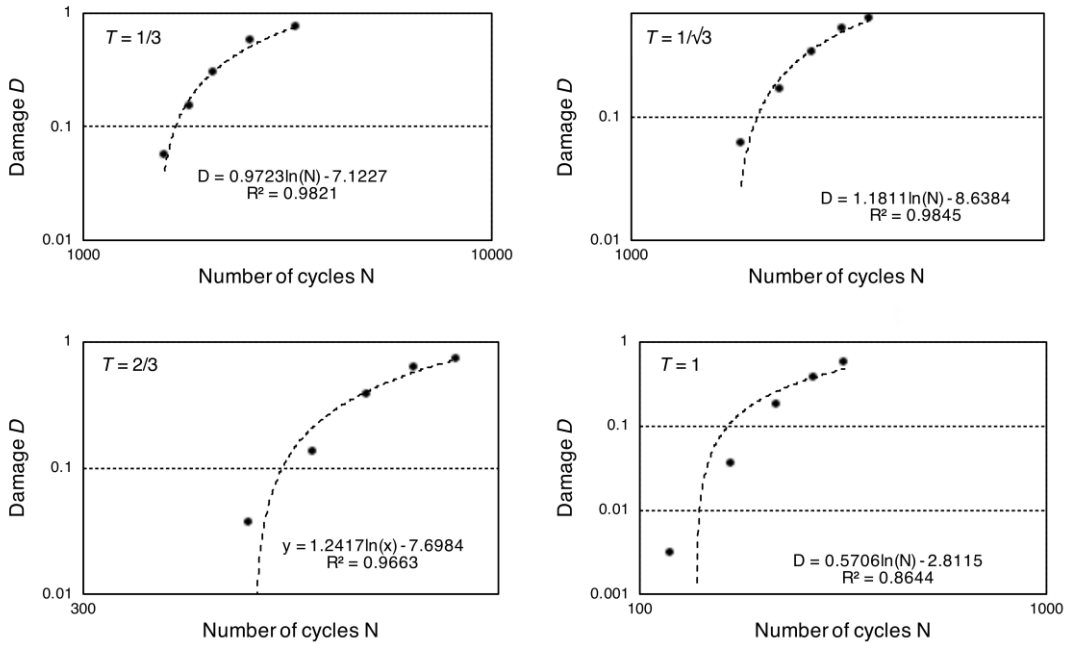

Fig. 4. Determination of damage evolution coefficients at strain amplitude 0.3% and different T.

K and K_0 are the current and initial stiffness, respectively, evaluated from the elastic part of the hysteresis cycle. Plotting D_{RVE} as a function of N, as illustrated in the examples of Fig. 4 for the strain amplitude 0.3 %, allows to evaluate $\frac{dD}{dN}\Big|_{RVE}$ which is then related to the corresponding ΔW for the various triaxialities, in order to find the coefficients $C_3(T)$, $C_4(T)$.

3.2. Round Notched Bar model (RNB)

A 2D-axisymmetric FE model is used to reproduce the LCF behavior of a circular notched bar capable of generate different triaxiality varying the notch radius, R. With reference to the Bridgman's equation [16], two different notch radii are here designed to vary T:

$$T = \frac{1}{3} + \ln\left(1 + \frac{a}{2R}\right) \tag{9}$$

with a is the radius at the notched cross section. The maximum of T develops at the center, but the highest strain amplitude develops at the notch root. The geometry of two models, namely A and B, is shown in Fig. 5, and relative dimensions are indicated in Tab. 3. The mesh, made of quad elements with reduced integration formulation, is set to have the element at the notch root of the same size of the RVE.

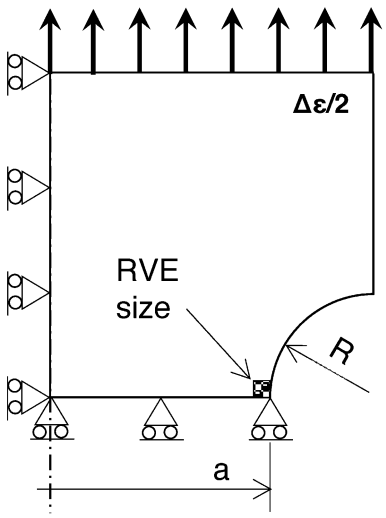

Fig. 5. Axisymmetric model of RNBs.

Tab. 3. Triaxialities of RNBs.

Model	D (mm)	a (mm)	R (mm)	T_{max}, Eq. (7)
A	20	5	5	0.74
B	20	7	3	1.11

Even RNB models are subjected to cyclic, strain-controlled loading. The homogenized RVE behavior is assumed as cyclic constitutive law, and the damage initiation and evolution are represented by Eq. (7) and (8), respectively. As the default ABAQUS© framework does not include a parameter dependence on triaxiality, Eqs. (7,8) are implemented using the ABAQUS© user subroutine USDFLD, which reads the values of ΔW and T from the results file and updates the value of $N_{0,RVE}$ at all the Integration Points (IPs) for each increment ΔN, until $N = N_{0,RVE}$. Thus, if the triaxiality at a IP changes during the simulation, the value of $N_{0,RVE}$ is being updated. Then the evolutionary part, Eq. (8), is started and D also is updated at every increment ΔN until the stiffness halves ($D = 0.5$). The choice of a critical $D = 0.5$ is coherent with the RVE damaged condition. As a result, the number of cycles at failure $N_{f,notch}$ is estimated for various deformation amplitudes. A theoretical number of cycles can be derived for RNBs by solving the system of equations represented by the Neuber's rule, Eq. (10), and the M-C-B curve of the RVE at $T = 1/3$ – Eq. (11) with Υ the RVE Young's modulus – and compared with the simulations revealing the impact of T on the fatigue life estimation in notched members:

$$\frac{\Delta\Sigma}{2}\frac{\Delta\mathrm{E}}{2} = \Upsilon\left(K_t\frac{\Delta\bar{\varepsilon}}{2}\right)^2 \tag{10}$$

$$\frac{\Delta\mathrm{E}}{2} = \frac{\bar{\sigma}_f'}{\Upsilon}\left(2N_f\right)^b + \bar{\varepsilon}_f'\left(2N_f\right)^c \tag{11}$$

4. Results and discussion

4.1. RVE response

The stabilized response of the RVE under the strain amplitude $\Delta E_1/2$ is illustrated by Fig. 6(a), for $T = 1/3$. Experimental results at $\Delta\varepsilon/2 = 0.6$ and 1.0% of the EN-GJS-400-18LT iron are also plotted [36]. The curves result comparable, indicating that the modeling approach and the nonlinear constitutive law

for the α-matrix are properly chosen. Due to the presence of rigid nodules, hysteresis loops are slightly unsymmetrical over the 1% of applied strain. Saturation of simulated plastic cycles occurs within 30–50 cycles showing hardening behavior, Fig. 6(b), which is also confirmed by experiments [37]; cyclic parameters of the Ramberg–Osgood form $E_a = E_{a,el} + E_{a,pl} = \Sigma_a/\mathrm{E} + (\Sigma_a/K')^{1/n'}$, which is also plotted, are $n' = 0.092$ and $K' = 603.2$, very close to the experimental ones [38]. For comparison, the equivalent plastic strain contours are plotted at three strain levels and for the 1st loading cycle, see Fig. 7, showing the influence of T on peak values and distribution within the microstructure.

The parameters of the homogenized nonlinear isotropic–kinematic model are obtained by fitting the results over the range of applied ΔE, using Eqs. (12,13), that is Eqs. (3,4) written in terms of mesoscale quantities:

$$\Sigma^0 = \Sigma|_0 + \Theta_\infty \left(1 - e^{-\beta \mathrm{E}^{pl}}\right) \tag{12}$$

$$\dot{\mathbf{A}} = \mathrm{X}\dot{\bar{\varepsilon}}^{pl} \frac{1}{\sigma^0}(\boldsymbol{\Sigma} - \mathbf{A}) - \Gamma \boldsymbol{\alpha} \dot{E}^{pl} \tag{13}$$

where the mesoscale equivalent plastic strain rate $\dot{\mathrm{E}}^{pl}$ is defined as $\dot{\mathrm{E}}^{pl} = \sqrt{\frac{2}{3}\dot{\mathbf{E}}^{pl}\dot{\mathbf{E}}^{pl}}$. These parameters are summarized in Tab. 4. These values will be used for the notched specimen models.

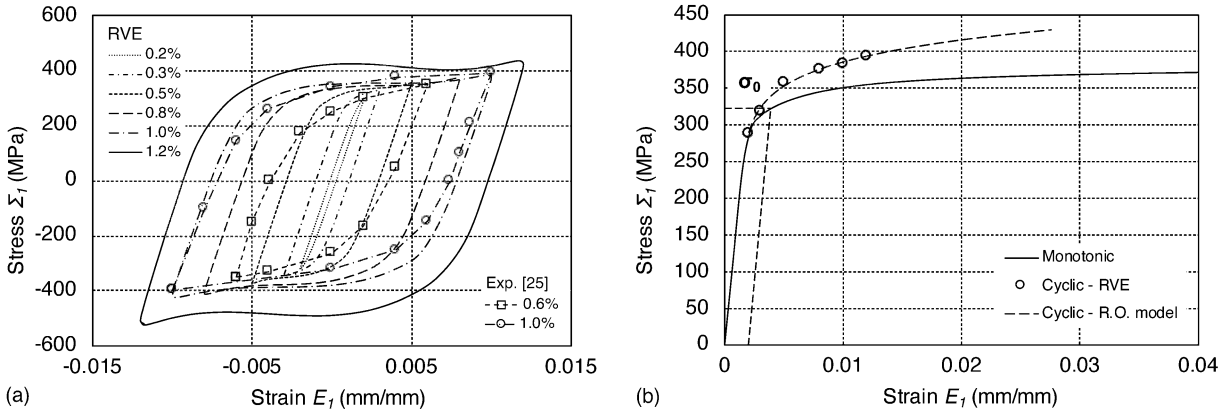

Fig. 6. (a) Stabilized $\Delta\Sigma$-ΔE curves at T=1/3; (b) RVE monotonic and cyclic curves.

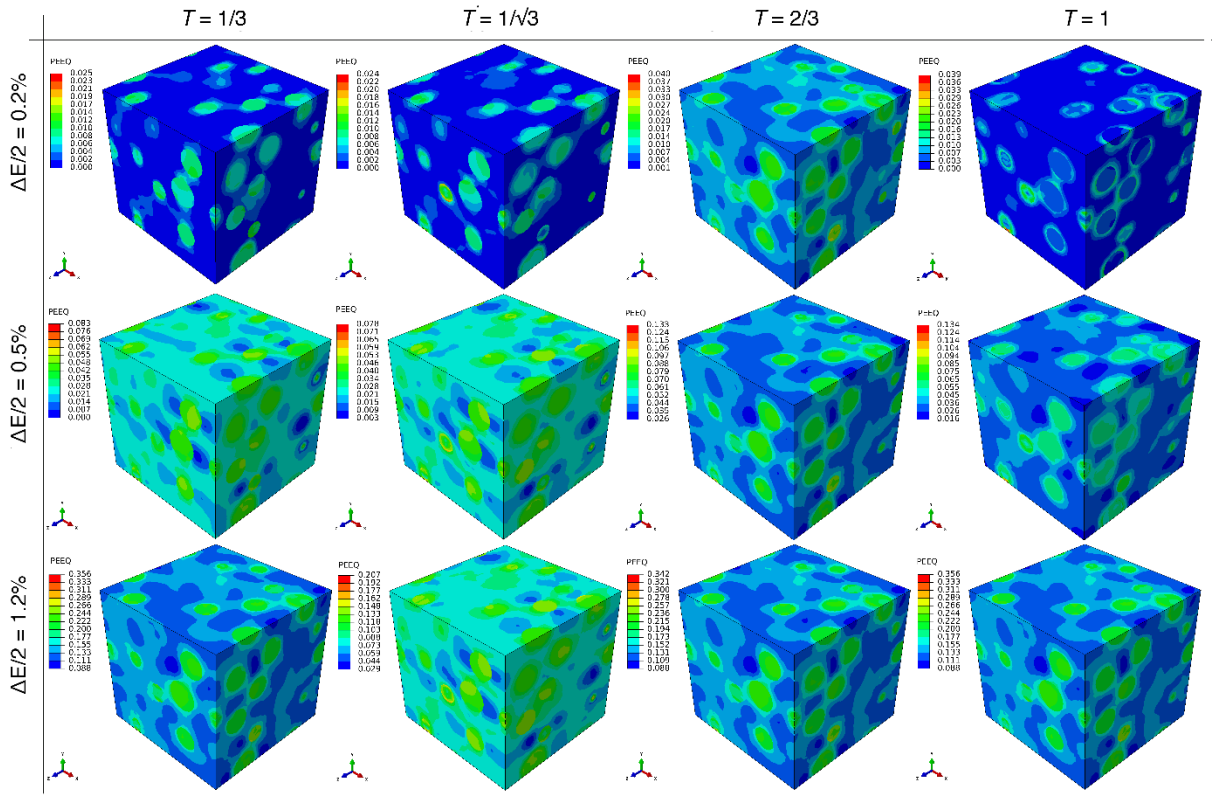

Fig. 7. Damage distribution in the RVE at 50% of stiffness (blue $D = 0$, red $D = 1$).

Tab. 4. Homogenized cyclic parameters of the DCI.

Y (GPa)	ν	$\Sigma\|_0$ (MPa)	Θ_∞ (MPa)	β	X (MPa)	Γ
171.2	0.31	323	32.9	3.37	4011	182.5

Simulations show that damage in the RVE originates at clusters of nodules; however, depending from T, maps of the damage variable D indicate that the quantity of elements reaching $D = 0.5$ is highly variable, as shown in Fig. 8 for 3 levels of strain amplitude corresponding to the 50% reduced stiffness. Accordingly, the higher the T the more rapidly the stiffness decrease; however, since the RVE is cycled in strain-control, the energy ΔW also decreases, and so the damage rate of Eq. (8). It means that a physical failure of the RVE can be even not reached.

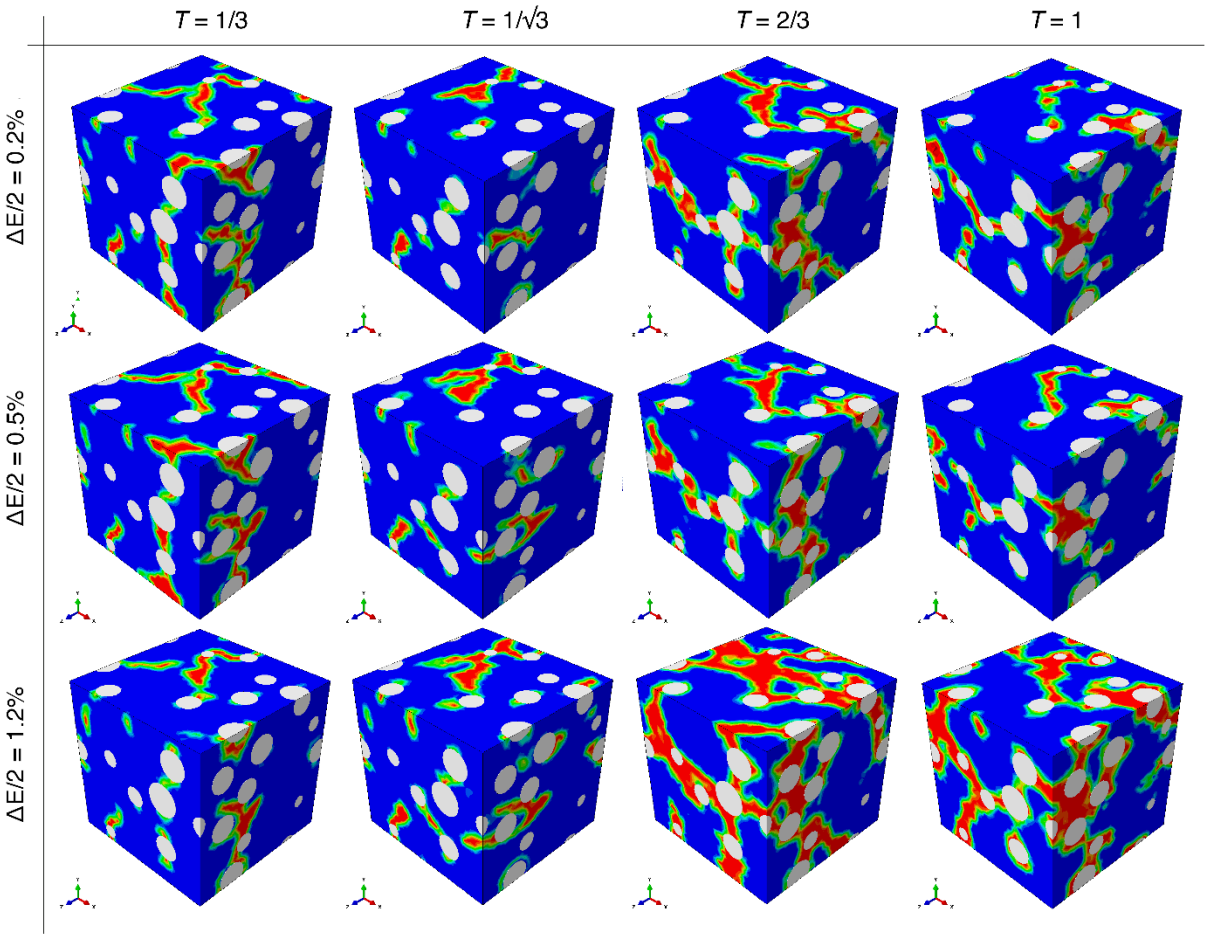

Fig. 8. Damage distribution in the RVE at 50% of stiffness (blue $D = 0$, red $D = 1$).

4.2. Effect of T on fatigue life and modified M-C-B law

Fatigue life curve for $T = 1/3$ is already shown having a very good correlation with the experimental tests on push-pull cylindrical specimens in the range $\Delta\varepsilon_a/2 = 0.2 \div 1.2\%$ and $N_f = 50 \div 100.000$ [23], while curves at different triaxiality, shown in Fig. 9(a), indicate the decreasing of life. Confirmation of such behavior can be found in the only experimental work on DCI published to date, to the authors knowledge, which still considers a ferritic-pearlitic matrix and a fatigue life from 10,000 cycles onwards [39]. The calculated fitting M-C-B parameters evidence that the slope of curves in elastic and plastic range slightly increases with T. Plots of Fig. 9(b) rationalize this main effect considering the life shortening in percentage with respect to the fatigue lifetime at $T = 1/3$: the effect is enhanced increasing the strain amplitude, thus plasticity, and is not linear with T. The dependance of fatigue life from T is

being rationalized defining an equivalent number of cycles to failure, N_f^*, which is function of T and of the applied strain amplitude. The modified M-C-B curve is defined following the classical form:

$$\frac{\Delta E_1}{2} = \frac{\Sigma'_f}{E}\left(2N_f^*\right)^{b'} + E'_f\left(2N_f^*\right)^{c'} \tag{14}$$

with the parameters Σ'_f = 626.5 MPa, E'_f = 1.51, b' = -0.0776, c' = -0.845, and the modified reversals to failure $2N_f^*$, that incorporates the contribution of T, is explicated as in Eq (15):

$$\frac{N_f^*}{N_f} = k_1 T^{k_2}$$

$$k_1 = 1.44\left(\frac{\Delta E_1}{2}\right)^{0.24};\ k_2 = 0.23 ln\left(\frac{\Delta E_1}{2}\right) + 0.376 \tag{15}$$

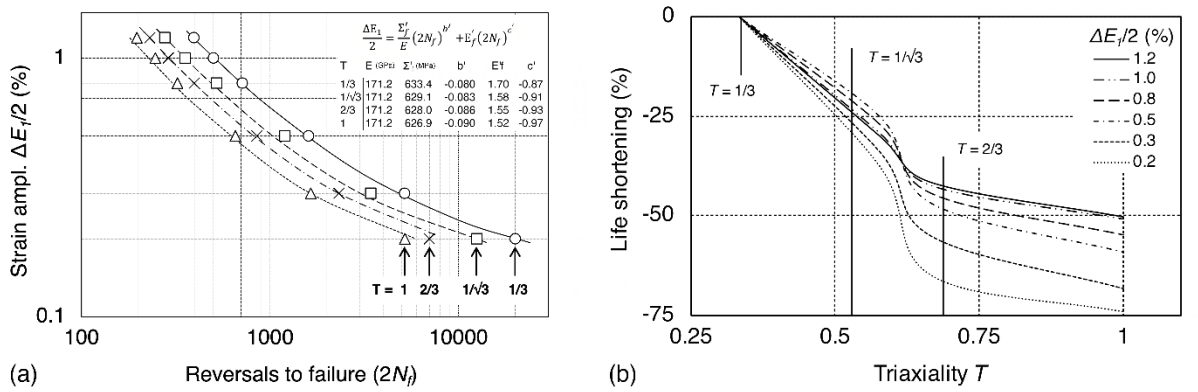

Fig. 9. (a) Fatigue life curves at various T (1 = axial direction); (b) effect of T on life shortening.

The relationship between N_f and N_f^* has been defined such that the curves on Fig. 9(a) at different triaxialities, when represented in terms of N_f^* collapse together in the *master curve* of Fig. 10. By Eq. (14) is then possible to account for the triaxiality effect when the stress state is different from the uniaxial tension. As previously said, this can be the case of a notched member.

Finally, following the procedure described in Section 3.1, the set of parameters C_1,…,C_4 controlling the damage initiation and evolution are calculated, see Tab. 5. The homogenized strain hysteresis energy ΔW per cycle is also determined from the analysis, see Fig. 11, which indicates the decisive effect of T in reducing the DCI fatigue life.

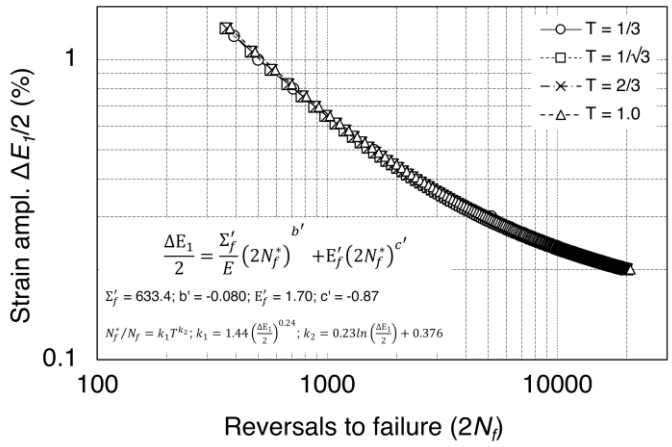

Fig. 10. Plot of modified M-C-B curve of Eqs. (14,15).

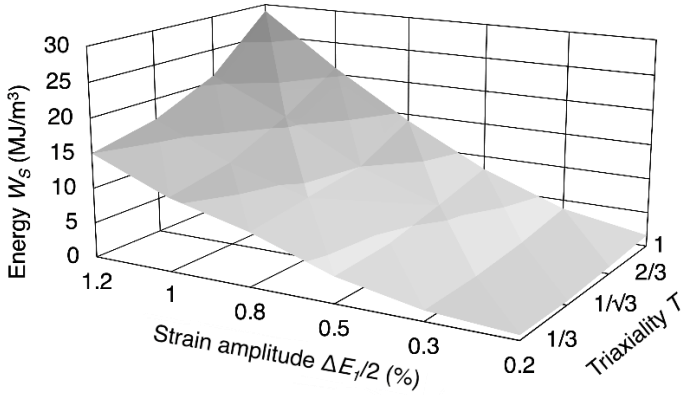

Fig. 11. Hysteresis energy ΔW vs. T at RVE failure.

4.3. Analysis by the notched specimens

The simulations on the two round bars with a circumferential groove are run with the material parameters of Tab. 5. As said, the effect of T on fatigue life is simulated by incorporating in the USDFLD ABAQUS© subroutine the same parameters and the surface plot in Fig. 11 for the hysteresis energy W. In other words, each element is allowed to have a different fatigue strength, depending on the strain amplitude and also on the level of triaxiality developed pointwise.

As known, strain concentration in the plastic regime at a notch can be described by the K_ε factor that appears in the Neuber's formula $K_t^2 = K_\sigma K_\varepsilon$ where K_t is the stress concentration factor in the elastic regime, K_σ and K_ε are the stress and strain concentration factors, respectively. Theoretical K_t for specimens A and B, which are $K_{t,A} = 1.48$, $K_{t,B} = 1.87$ in the elastic regime, switch into the K_ε factors of Tab. 6 in the plastic regime, calculated with Neuber's hyperbole on the cyclic curve.

Tab. 5. Parameters of Eqs. (7,8).

T	C_1	C_2	C_3	C_4
1/3	3330	-1.09	$4.2 \cdot 10^{-4}$	0.358
√3/3	2840	-1.14	$5.2 \cdot 10^{-4}$	0.395
2/3	2120	-1.17	$6.3 \cdot 10^{-4}$	0.512
1	1740	-1.21	$7.4 \cdot 10^{-4}$	0.719

Considering these K_ε, appropriate displacements are applied to the RNB boundaries to obtain, at the notch root, the same strain amplitude of the RVE (0.2–1.2 %). In the bars, T is maximum at the axis and strain at the notch, hence failure is typically determined by a concurrent mechanism in IPs across the net section. At each IP, the USDFLD subroutine considers the resulting energy of the hysteresis cycle and set the number of cycles to initiation correspondingly to Eq. (8), determining the evolution of D until failure. Simulations show how some of the failures initiate at the notch and progress to the center, as shown in Fig. 12; however, the evolution of damage is very similar between the models.

Tab. 6. Concentration factors on the strain amplitude.

Model	K_t	K_ε				
		$\Delta\varepsilon_a/2$ (%)	0.1	0.15	0.2	0.3	0.4
A	1.48		1.10	1.64	2.19	3.29	4.38
B	1.87		1.75	2.62	3.50	5.24	6.99

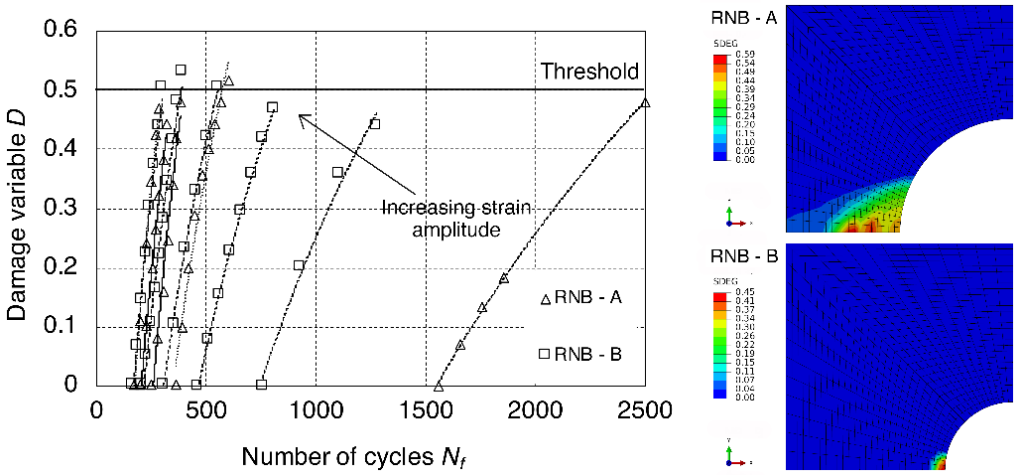

Fig. 12. Damage initiation and evolution in the RNB models.

In Fig. 13 the results of RNB simulations are compared with those resulting from applying Eq. (14) which is found by the RVE calculation, and with those coming from Neuber's rule theoretical analysis – Eqs. (10,11). In Eq. (14), the value of T is taken at the notch root of RNB, before damage initiation. Concerning Neuber's rule, the nominal strain amplitude is taken as reference in the plot, the effective strain at the notch root is analytically calculated from that by the K_ε factors, and the reversals to failure are calculated by Eq. (11), where the influence of triaxiality has been accounted for by the correction to $2N_f$ explicated in Eq. (15). The outcome of the comparison indicates that all the data point are included into a narrow band, with FEM simulations of RNB showing just a bit lower fatigue strength at the higher number of cycles, i.e., where elastic strain is not negligible. It has to be noted that, if the contribution of T would not be taken into account in the theoretical analysis, the results of Neuber's rule would diverge consistently. Therefore, it can be stated that T has a noticeable impact on the LCF strength of DCI, that can be effectively captured by the present microstructural, multilevel simulation approach.

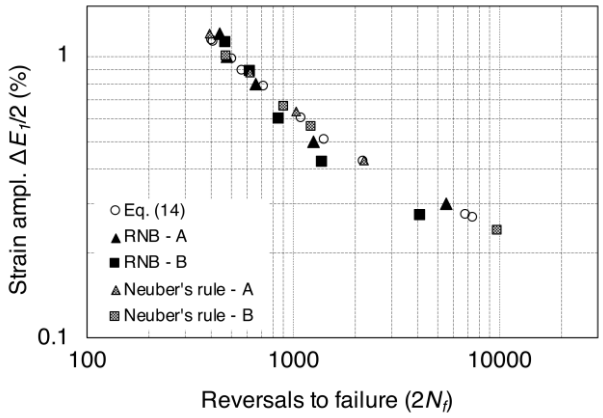

Fig. 13. Comparison of fatigue life curves for the RVE, notched bars, and estimated by the Neuber's rule (see Fig. 3).

5. Conclusions

A stochastic, micromechanical RVE model of the DCI material system is cyclically loaded by strain-controlled loads, imposing various values of stress triaxiality; together with the plastic strain level, this causes considerable gradients of the triaxiality at the local-microstructural scale. The RVE analysis also

yielded a triaxiality dependent Manson-Coffin-Basquin curve at the mesoscale level, that is used as an input for the following simulation of two RNB geometries having different notch radii, and triaxialities. The RNB material model is also coming from the RVE and accounts for triaxiality effects: this is the macro-scale response. From the investigation, some interesting conclusions can be drawn:

1. a triaxiality distribution within the RVE is naturally generated by the peculiar microstructure of DCI, and magnifies the effect of the stress triaxiality imposed at the meso-scale;
2. a stress triaxiality higher than 1/3 at the mesoscale increases the cyclic plastic strain amplitude of the RVE, reducing the fatigue life;
3. a homogenized LCF behavior of the DCI in terms of cyclic stress-strain response and a new M-C-B equation are obtained as a function of the triaxiality T; qualitative confirmation of the T effect is found in [39];
4. the homogenized behavior applied to the simulations on RNBs yield a competition between triaxiality and strain concentration at the notch root in the nucleation and growth of a crack;
5. a comparison of fatigue life estimated with the RNB model and the analytical Neuber's rule confirms that the homogenization approach adopted in this work is an effective in estimating the fatigue life of DCI notched components.
6. ~~finally, an experimental campaign on samples capable of generating different triaxialities is foreseen to validate the results of the simulations.~~

References

[1] https://www.caef.eu/statistics/

[2] Ganjiani M., Homayounfard M. Development of a ductile failure model sensitive to stress triaxiality and Lode angle. International Journal of Solids and Structures 2021;225:111066

[3] Anderson D., Winkler S., Bardelcik A., Worswick M.J. Influence of stress triaxiality and strain rate on the failure behavior of a dual-phase DP780 steel. Materials & Design 2014;60:198–207.

[4] Bao Y., Wierzbicki T. On fracture locus in the equivalent strain and stress triaxiality space. International Journal of Mechanical Sciences 2004;46:81–98.

[5] Danas K., Ponte Castañeda P. Influence of the Lode parameter and the stress triaxiality on the failure of elasto-plastic porous materials. International Journal of Solids and Structures 2012;49:1325–1342.

[6] Pirondi A., Bonora N., Steglich D., Brocks W., Hellmann D. Simulation of failure under cyclic plastic loading by damage models. International Journal of Plasticity 2006;22(11):2146–2170.

[7] Bonora N., Gentile D., Pirondi A., Newaz G. Ductile damage evolution under triaxial state of stress: theory and experiments. International Journal of Plasticity 2005;21(5):981–1007.

[8] Warmuzek M., Polkowska A. Micromechanism of damage of the graphite spheroid in the nodular cast iron during static tensile test. Journal of Manufacturing and Materials Processing 2020;4(1):22.

[9] Di Cocco V., Iacoviello D., Iacoviello F., Rossi A. Graphite nodule influence on DCIs mechanical properties: experimental and numerical investigation. Procedia Engineering 2015;109:135–143.

[10] Collini L., Pirondi A., Bianchi R., Cova M., Milella P.P. Influence of casting defects on fatigue crack initiation and fatigue limit of ductile cast Iron. Procedia Engineering 2011;10:2898–2903.

[11] Nicoletto G., Collini L., Konecna R., Riva E. Analysis of nodular cast iron microstructures for micromechanical model development. Strain 2006;42(2):89–96.

[12] Yanagisawa O., Lui T.S. Influence of the structure on the 673 K embrittlement of ferritic spheroidal graphite cast iron. Trans Japan Inst Metals 1983;24(12):858–867.

[13] Collini L., Moroni F., Pirondi A. Modeling the influence of stress triaxiality on the failure strain of nodular cast iron microstructures. Procedia Structural Integrity 2019;18:671–687.

[14] Collini L., Pirondi, A. Micromechanical modeling of the effect of stress triaxiality on the strain to failure of ductile cast iron. Engineering Fracture Mechanics 2020;238,107270.

[15] Liu Z.G., Wong W.H., Guo T.F. Void behaviors from low to high triaxialities: Transition from void collapse to void coalescence. International Journal of Plasticity 2016;84:183–202.

[16] Bridgman P.W. Studies in large plastic flow and fracture. 1952, McGraw-Hill, New York.

[17] Lin Y.F., Lui T.S., L. H. Chen. The effect of triaxial stress on ductility and fracture morphology of ferritic spheroidal graphite cast iron. Metallic Materials Transactions A 1994;25(4):821–825.

[18] Lin R.C., Steglich D., Brocks W., Betten J. Performing RVE calculations under constant stress triaxiality for monotonous and cyclic loading. International Journal for Numerical Methods in Engineering 2006;66:1331–1360.

[19] Rabold F., Kuna M., Cell model simulation of void growth in nodular cast iron under cyclic loading. Computational Materials Science 2005;32:489–497.

[20] Lukhi M., Kuna M., Hütter G. Numerical investigation of low cycle fatigue mechanism in nodular cast iron. International Journal of Fatigue 2018;113:290–298.

[21] Kiran R., Khandelwal K. A micromechanical cyclic void growth model for ultra-low cycle fatigue. International Journal of Fatigue 2015;70:24–37.

[22] Collini, L., F., Pirondi, A. Microstructure-based RVE modeling of the failure behavior and LCF resistance of ductile cast iron. Procedia Structural Integrity 2019;24:324–336.

[23] Lemaitre J., Chaboche J.-L. Mechanics of Solid Materials, Cambridge University Press, 1990.

[24] White C.S. A combined isotropic-kinematic hardening model for large deformation metal plasticity. MTL TR 88-46, Watertown MA, 1988.

[25] Lemaitre J. A Course on Damage Mechanics. Springer, Berlin, 1996.

[26] Darveaux R. Effect of simulation methodology on solder joint crack growth correlation and fatigue life prediction. Journal of Electronic Packaging 2002;124:147–154.

[27] Younghune K., Woonbong H. High-Cycle, Low-Cycle, Extremely Low-Cycle fatigue and monotonic fracture behaviors of low-carbon steel and its welded joint. Materials 2019;12(24),4111.

[28] Komotori J., Shimizu M. Fracture mechanism of ferritic ductile cast iron in extremely low cycle fatigue. In: Rie K.-T., Portella P.D., editors. Low cycle fatigue and elasto-plastic behaviour of materials. Netherlands: Springer; 1998:39–44.

[29] Andriollo T., Hattel J. On the isotropic elastic constants of graphite nodules in ductile cast iron: Analytical and numerical micromechanical investigations. Mechanics of Materials 2016;96:138–150.

[30] Di Cocco V., Iacoviello F., Rossi A. Stress triaxiality influence on damaging micromechanisms in a pearlitic ductile cast iron. Frattura ed Integrità Strutturale 2014;8(40):462–468.

[31] Zhang Y.B., Andriollo T., Fæster S., Barabash R., Xu R., Tiedje N., Thorborg J., Hattel J., Juul Jensen D., Hansen N. Microstructure and residual elastic strain at graphite nodules in ductile cast iron analyzed by synchrotron X-ray microdiffraction. Acta Materialia 2019;167(1):221–230.

[32] Bonora N., Ruggiero A. Micromechanical modeling of ductile cast iron incorporating damage. Part I: Ferritic ductile cast iron International Journal of Solids and Structures 2005;42(5–6):1401–1424.

[33] Andriollo T., Fæster S., Winther G. Probing the structure and mechanical properties of the graphite nodules inductile cast irons via nano-indentation. Mechanics of Materials 2018;122:85–95.

[34] Fernandino D.O., Cisilino A.P., Boeri R.E. Determination of effective elastic properties of ferritic ductile cast iron by computational homogenization, micrographs and microindentation tests. Mechanics of Materials 2015;83:110–121.

[35] Coffin L.F. The flow and fracture of a brittle material. Journal of Applied Mechanics 1950;72:233–248.

[36] Canzar P., Tonkovic Z., Kodvanj J. Microstructure influence on fatigue behaviour of nodular cast iron. Materials Science and Engineering 2012;A556:88–99.

[37] Guillemer-Neel C., Bobet V., Clavel M. Cyclic deformation behaviour and Bauschinger effect in ductile cast iron. Materials Science and Engineering 1999;A272:431–442.

[38] Hesseler J., Baumgartner J., Bleicher C. Consideration of the transient material behavior under variable amplitude loading in the fatigue assessment of nodular cast iron using the strain-life approach. Fatigue and Fracture of Engineering Materials and Structures 2021;44(10);2845–2857.

[39] Benedetti M., Santus C., Raghavendra S., Lusuardi D., Zanini F., Carmignato S. Multiaxial plain and notch fatigue strength of thick-walled ductile cast iron EN-GJS-600-3: Combining multiaxial fatigue criteria, theory of critical distances, and defect sensitivity. International Journal of Fatigue 156 (2022) 106703